Structure of magma reservoirs beneath Merapi and surrounding volcanic centers of Central Java modeled from ambient noise tomography

Ivan Koulakov, Gulzhamal Maksotova, Kayrly Jaxybulatov, Ekaterina Kasatkina, Nikolai M. Shapiro, Birger-G. Luehr, Sami El Khrepy, Nassir Al-Arifi

AGU PUBLICATIONS

Geochemistry, Geophysics, Geosystems

RESEARCH ARTICLE
10.1002/2016GC006442

Key Points:
- We present a new high-resolution 3-D seismic model of the crust beneath Central Java derived from ambient noise tomography inversion
- We can distinguish anomalies associated with a shallow sediment layer and deeper crustal magma storage feeding Merapi and other volcanoes
- Body and surface wave tomographies reveal a multilevel pathway of melts and volatiles from the slab to the shallow magma reservoir of Merapi

Correspondence to:
I. Koulakov,
ivan.science@gmail.com

Citation:
Koulakov, I., G. Maksotova, K. Jaxybulatov, E. Kasatkina, N. M. Shapiro, B.-G. Luehr, S. El Khrepy, and N. Al-Arifi (2016), Structure of magma reservoirs beneath Merapi and surrounding volcanic centers of Central Java modeled from ambient noise tomography, *Geochem. Geophys. Geosyst.*, *17*, 4195–4211, doi:10.1002/2016GC006442.

Received 17 MAY 2016
Accepted 30 SEP 2016
Accepted article online 4 OCT 2016
Published online 27 OCT 2016

Structure of magma reservoirs beneath Merapi and surrounding volcanic centers of Central Java modeled from ambient noise tomography

Ivan Koulakov[1,2], Gulzhamal Maksotova[1,3], Kayrly Jaxybulatov[1,4], Ekaterina Kasatkina[1,2], Nikolai M. Shapiro[4,5], Birger-G. Luehr[6], Sami El Khrepy[7,8], and Nassir Al-Arifi[7]

[1]Trofimuk Institute of Petroleum Geology and Geophysics SB RAS, Novosibirsk, Russia, [2]Novosibirsk State University, Novosibirsk, Russia, [3]Kazakh Petroleum Institute of Scientific Research and Geological Survey (KazNIGRI), Atyrau, Kazakhstan, [4]Institut de Physique du Globe de Paris, Sorbonne Paris Cité, CNRS (UMR 7154), 1 rue Jussieu, Paris, France, [5]Institute of Volcanology and Seismology, FEB RAS, Kamchatsky Region, Russia, [6]Deutsches GeoForschungsZentrum GFZ, Potsdam, Germany, [7]King Saud University, Riyadh, Saudi Arabia, Riyadh, Saudi Arabia, [8]National Research Institute of Astronomy and Geophysics, NRIAG, Helwan, Egypt

Abstract We present a three-dimensional model of the distribution of S-wave velocity in the upper crust to a depth of 20 km beneath Central Java based on the analysis of seismic ambient noise data recorded by more than 100 seismic stations in 2004 associated with the MERAMEX project. To invert the Rayleigh wave dispersion curves to construct 2-D group-velocity maps and 3-D distributions of S-wave velocity, we have used a new tomographic algorithm based on iterative linearized inversion. We have performed a series of synthetic tests that demonstrate significantly higher resolution in the upper crust with this model compared to the local earthquake travel-time tomography (LET) model previously applied for the same station network. Beneath the southern flank of Merapi, we identify a large low-velocity anomaly that can be split into two layers. The upper layer reflects the ~1 km thick sedimentary cover of volcanoclastic deposits. The deeper anomaly at depths of ~4–8 km may represent a magma reservoir with partially molten rock that feeds several volcanoes in Central Java. Beneath the Merapi summit, we observe another low-velocity anomaly as deep as 8 km that may be associated with the active magma reservoir that feeds the eruptive activity of Merapi. In the southern portion of the study area, in the lower crust, we identify a low-velocity anomaly that may represent the top of the pathways of volatiles and melts ascending from the slab that was previously inferred from the LET model results. We observe that this anomaly is clearly separate from the felsic magma reservoirs in the upper crust.

1. Introduction

Central Java (Figure 1) is one of the world's most densely populated areas, and it suffers significantly from seismic and volcanic hazards. Mt. Merapi ("Fire Mountain" in Javanese) is the most active volcano in Indonesia; it has erupted fairly regularly since at least 1560 [e.g., *Voight et al.*, 2000]. Pyroclastic flows from Merapi threaten thousands of people who live in villages surrounding the volcano, as well as the densely populated city of Yogyakarta 25 km to the south, which has a population of over 2.4 million in its metropolitan area. The episodic eruptions of Merapi necessitate large-scale evacuations of the communities on its flanks. In 1994, a large pyroclastic flow caused by a dome collapse killed 64 people in the village of Turgo on the volcano's southern flank. In 2006, an eruption occurred almost synchronously with the M6.4 Yogyakarta Earthquake, which had a death toll of over 5,700. It is still debated whether these two events were connected, or if their close occurrence in space and time was coincidental [e.g., *Walter et al.*, 2007; *Troll et al.*, 2012]. Approximately 25,000 residents were displaced, mainly from the areas that were most strongly affected by the earthquake. The most recent major eruption of Merapi occurred on 25 October 2010, which required the evacuation of over a quarter of a million people from within a radius of ~20 km from the volcano's summit [*Jousset et al.*, 2012].

Other volcanoes in central Java are also considered to be potentially active. Although presently they do not exhibit the strong and frequent volcanic activity of Mt. Merapi, there is substantial evidence for ongoing

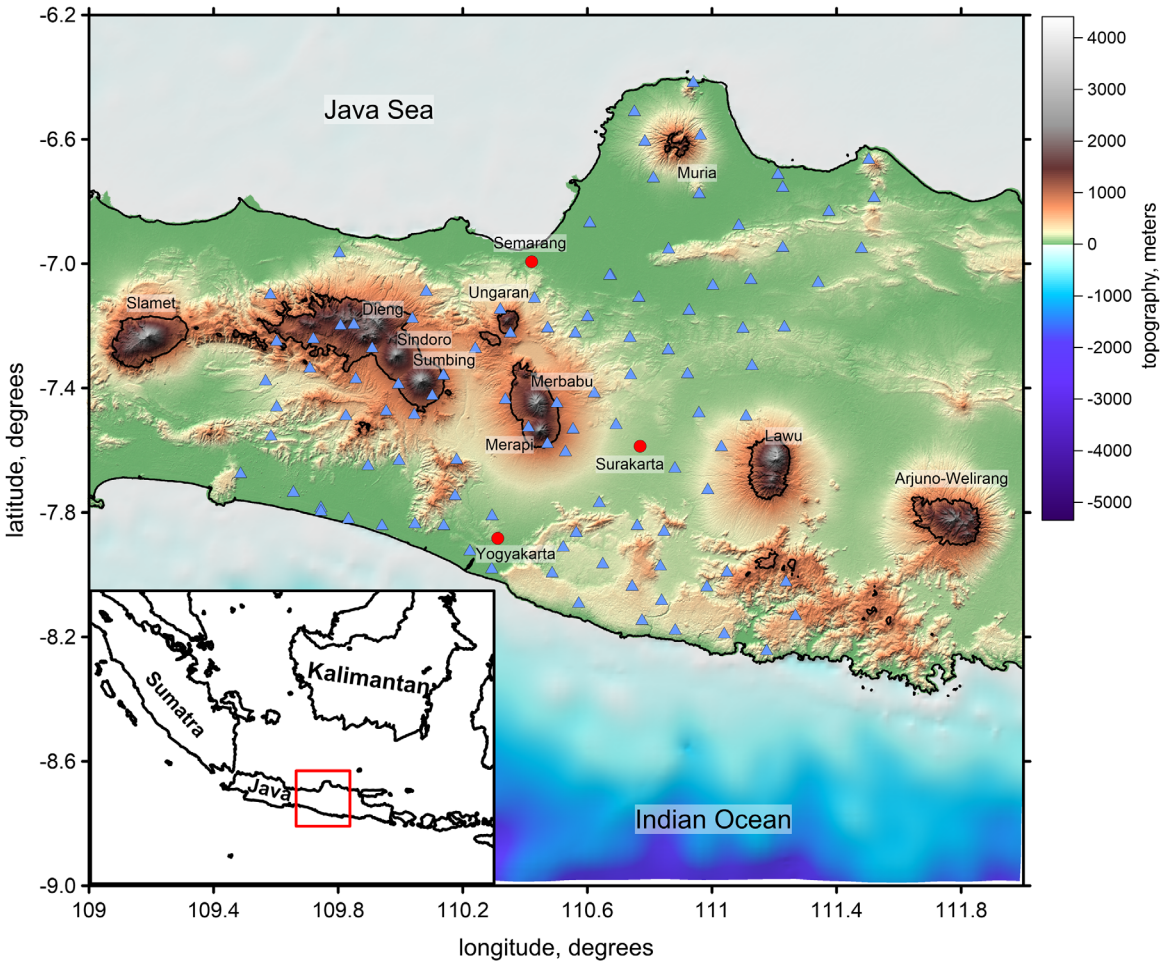

Figure 1. Topographic map of the study area from www.marine-geo.org. The contour line for 1000 m altitude is shown. Blue triangles indicate the seismic stations used in this study. Red dots indicate the major cities in the study area. Inset shows the location of the study area.

processes in other magma systems, such as fumarolic and seismic activity. For example, for Mt. Merbabu, which is located in the same volcanic chain as Mt. Merapi and is presently considered dormant, there are historical records of at least two moderate eruptions: one in 1560 and another in 1797 [*Simkin and Siebert*, 1994]. There is evidence that an eruption of Mt. Sumbing in 1730 created a small phreatic crater. Mt. Sindoro is also considered to be potentially dangerous because it episodically shows increases in fumarolic activity and volcano-tectonic seismicity. Mt. Lawu, located east of Merapi, has not had a strong eruption since before the Holocene [*Siebert et al*., 2010]; nevertheless, episodic swarms of seismicity and fumaroles indicate its potential danger as well.

Each of these active and dormant volcanoes in Central Java may represent real risks for the populations of the region. Therefore, detailed investigation of crustal and mantle structure beneath Java is critical for understanding the mechanisms of magma transport and assessing the hazards of future eruptions.

The Central Java area has been thoroughly studied through the analysis of the extensive data set collected by the MERAMEX (MERapi AMphibious EXperiment) project initiated by the GFZ German Research Centre for Geosciences and financed by the German Federal Ministry of Education and Research [*Koulakov et al*., 2007]. The seismological component of this project included the deployment of more than 100 seismic stations onshore and offshore in the Central Java area. In addition to these passive source studies, active source seismic surveys were conducted in the offshore areas, which have provided important complementary information. These data have already been used in several tomographic studies. The first model based on this data set was reported by *Koulakov et al*. [2007], who found a large low-velocity anomaly in the

region between the Merapi and Lawu volcanoes. The data set was then complemented with active source data that improved resolution in the offshore and forearc areas [*Wagner et al*., 2007]. Later, analysis of anisotropic tomography by *Koulakov et al*. [2009] also revealed the existence of this crustal low-velocity anomaly, as well as an inclined low-velocity root dipping toward the subducting slab. Similar features were later identified using algorithms for travel-time tomography [*Haberland et al*., 2014] and attenuation tomography [*Bohm et al*., 2013]. This large crustal low-velocity and high-attenuation anomaly is also apparent in the gravity field. Joint modeling with the use of seismic and gravity data has revealed a strong low-density anomaly in the crust beneath this region [*Luehr et al*., 2013].

The results of these studies suggest that the volcanoes of Central Java are fed by ascending fluids and melts generated by mineralogical phase transitions in the subducting slab. A large low-velocity anomaly in the crust with a magnitude as high as 30% was proposed to indicate a large magma reservoir that feeds all volcanoes in Central Java including Mt. Merapi. However, there have been doubts about the inferred depth and location of this anomaly because of the dominantly vertical orientations of the seismic rays used in the tomographic inversions based on body waves from earthquakes. Some opponents have suggested that this anomaly may merely be a result of downward smearing of low-velocity sediment cover in the Kendeng basin to the northeast of Merapi, which may be very thick in this area because of long-term deposition of pyroclastics. If this alternative were the case, the above hypothesis of a large crustal reservoir would be invalid. Unfortunately, the body-wave tomography alone cannot confirm or disprove either interpretation because of its limited vertical resolution.

For this reason, surface-wave tomography, which has higher vertical resolution within shallow layers, may yield valuable complementary information about the depth distributions of the sedimentary cover and magmatic structures. The relatively dense and uniform distribution of the seismic stations makes them suitable for ambient noise tomography. The first attempt to use ambient noise tomography with the MERAMEX data from Central Java was performed by *Zulfakriza et al*. [2014]. They reported the presence of the same crustal low-velocity anomaly that was detected in the previous tomographic studies; however, the image was strongly perturbed by small, patchy patterns that were likely associated with noise, possibly because of insufficient stability of a transdimensional inversion technique used in that study. Therefore, we have chosen to revisit the data set and to perform a complete analysis using algorithms we have developed. We have identified clear structures that corroborate previous findings, and continue the discussion of the magma plumbing system of Central Java.

2. Description of the Data

The MERAMEX Project was launched in 2004 for detailed investigation of the crustal and uppermost mantle structures beneath Central Java [*Koulakov et al*., 2007]. The seismological component of the project consisted of the deployment of 134 seismic stations: 106 short-period stations, 14 broadband stations, eight ocean bottom hydrophones (OBH) and six ocean bottom seismometers (OBS). Onshore, the average spacing between stations was approximately 25 km. The network covered an area of 200 $\times$ 250 km. Most of these stations recorded continuously for $\sim$150 days from May to October 2004.

Here, we have used records only of the identical short-period onshore stations (Mark-L4) at the locations indicated in Figure 1. Although the stations had the declared lower frequency of 1 Hz, the Mark Products L-4 sensors ensures lower-frequency limit of sensitivity at approximately 0.06 Hz [*Riedesel et al*., 1990]. Continuous seismograms were recorded in the SEED format with a sampling rate of 100 Hz, for approximately 350 Gb of data in total. For this study, we used only records of the vertical seismic component to provide Rayleigh wave information.

3. Cross Correlation of the Ambient Seismic Noise

We applied noise-based surface-wave seismic tomography [e.g., *Shapiro et al*., 2005; *Ritzwoller et al*., 2011] by extracting the surface-wave components of the Green's functions from cross-correlations of the ambient seismic noise [e.g., *Shapiro and Campillo*, 2004; *Campillo et al*., 2011]. The preliminary processing of the data for ambient noise tomography was performed following to the procedure described by *Bensen et al*. [2007]. Because we used identical stations, we did not include any instrumental corrections. In the first stage, we organized the continuous seismograms into 24 h segments and converted them into mSEED format. Next, the

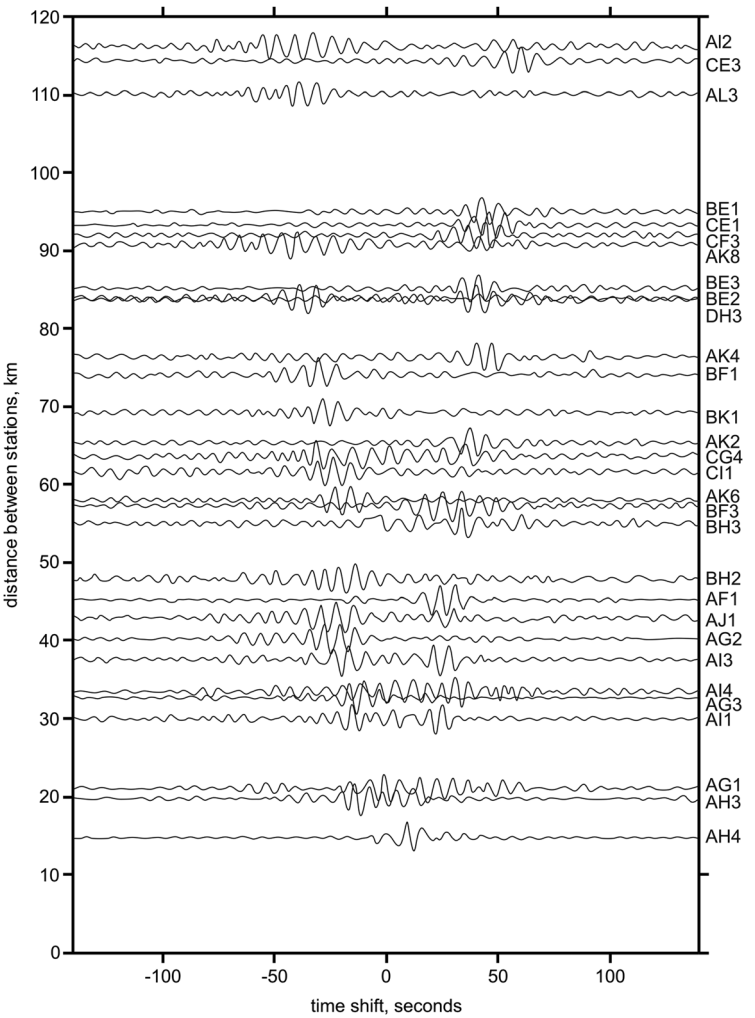

Figure 2. Example of cross correlation for the station AH2 with stations ranged according to the distance. The signal is filtered in band-pass frequencies between 0.1 and 0.2 Hz.

sampling rate was reduced from 100 to 10 Hz. We then performed spectral whitening using a series of narrow-band filters in a range of periods from 1 s to 15 s with increments of 1 s. This step reduced the effects of possible monochromatic signal sources. To remove the effect of large-amplitude signals associated with local impacts and earthquakes, we performed one-bit normalization that removed amplitude information and left only phase information.

The surface-wave information was retrieved through cross-correlation of the seismic signals for all possible pairs of seismic stations. With 106 available stations, in our case there were 5565 pairs to be analyzed. We cross-correlated the 24 h records with the shifting range of $\pm$ 150 s that exceeds possible values for travel times of surface waves between any pair of stations in the MERAMEX network. To improve the signal-to-noise ratio, we stacked the derived daily correlograms for the entire recording period. An example of the computed cross-correlations is shown in Figure 2. We summed the positive and negative parts of the cross-correlograms to extract the symmetric components.

We then conducted the frequency-time analysis developed for surface-wave processing by *Levshin et al.* [1989] and *Ritzwoller and Levshin* [1998] to measure group-velocity dispersion curves. An example of such measurement is shown in Figure 3.

For tomography, we selected group-velocity values according to several criteria: (1) the signal-to-noise ratio should be more than three; (2) the group velocity for each period should not deviate from the average value more than twice; (3) the distance between stations should be over 50% larger than the wavelength; (4) the difference in group velocities measured from the positive and the negative parts of the correlograms must not exceed 100 m/s. Based on these four criteria, we have selected dispersion curves with numbers indicated in Table 1. Large numbers of satisfactory data were obtained for the range of periods from 3 to 7 s. The amount of data drastically decreased with larger periods. For example, for the period of 15 s, only 29 station pairs met the criteria to be selected. In Figure 4a, we present the 939 ray paths that correspond to the period of 7 s.

4. Algorithms for Tomography Inversion

We have developed an algorithm for calculations of 2-D maps of group velocities and 3-D distributions of shear-wave velocities based on the inversion of dispersion curves. This algorithm is based on a concept of

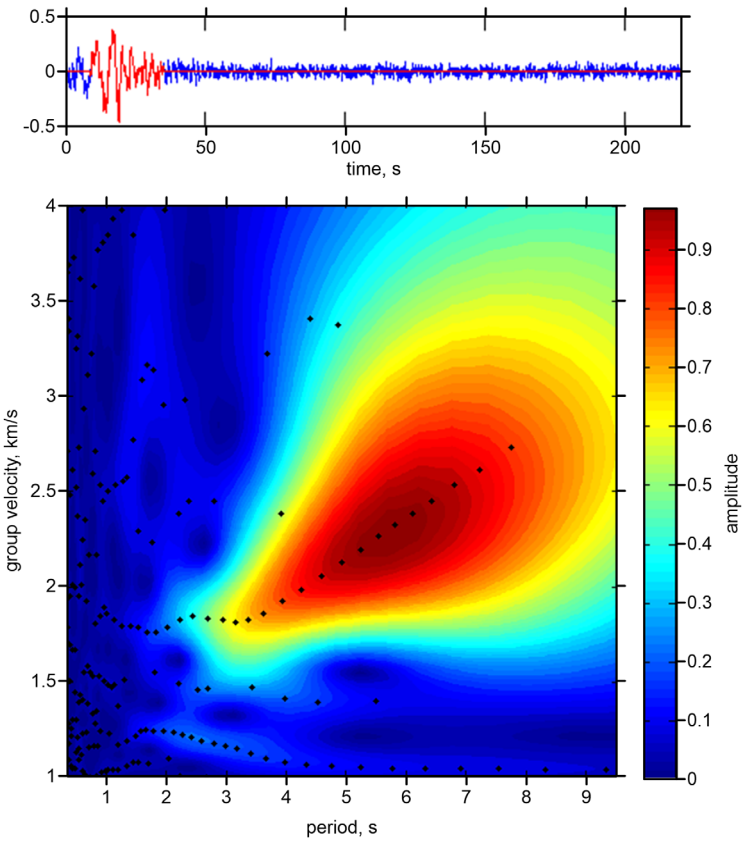

Figure 3. Example of the dispersion curve picking at stations AK8 and BJ2 located at the distance of 35.7 km. (top) Rhe Green function for the vertical component seismogram. Red highlights the part, which is processed by the time-frequency analysis. (bottom) The Green function energy depending on the period. Dots indicate all possible dispersion curves.

iterative linearized inversion, in contrast to the widely-used Monte-Carlo-based schemes [e.g., *Shapiro and Ritzwoller*, 2002]. Although linearized approaches have been used in previous studies [e.g., *Macquet et al.*, 2014; *Zhang et al.*, 2014], in our system, we implemented parts of the tomographic engine that were previously successfully tested in existing software, such as LOTOS [*Koulakov*, 2009]. Here we present a detailed, step-by-step description of the new algorithm.

The input data for this algorithm were files with group velocities for fixed frequencies corresponding to all selected station pairs. In total, we used fourteen files corresponding to periods from 2 to 14 s in increments of 1 s. The number of pairs and average group velocity and average deviations in the L1 norm for each period are presented in Table 1.

4.1. Two-Dimensional Tomography for Group Velocities

The two-dimensional distributions of group velocities were computed based on the iterative tomographic inversion of the group-velocity data for all available station pairs. Due to large expected variations of seismic anomalies in the study area, the inverse tomographic problem becomes significantly nonlinear. An important issue in the case of iterative solving this problem is related to using a fast and stable algorithm for kinematic modeling the surface wave propagation. In some studies, this problem is solved using an eikonal solver. For example, *Lin et al.* [2009], constructed the phase velocity map by solving the eikonal equations using travel time surface. In this case, they did not use ray paths to perform the tomography inversion. Similar principle, but with different practical realization has been implemented by *Young et al.* [2011]. *Fang et al.* [2015] directly inverted all dispersion data for 3-D *Vs* structures by iteratively updating the ray paths with an eikonal solver.

Table 1. Number of Source-Receiver (SR) Pairs and Average Group Velocities for Each of the 14 Periods Used for Tomography

Period (s)	Number of SR Pairs	Average Group Velocity (km/s)	Average Deviation in L1 Norm, (km/s)
2	834	1.99	0.318
3	1002	2.04	0.308
4	1054	2.06	0.300
5	1057	2.11	0.298
6	1016	2.16	0.300
7	939	2.24	0.307
8	698	2.30	0.317
9	430	2.36	0.323
10	248	2.40	0.318
11	152	2.42	0.310
12	89	2.47	0.334
13	60	2.49	0.348
14	42	2.51	0.333
15	29	2.53	0.318

We have developed a new algorithm of ray tracing, which uses the Fermat principle of travel time minimization and called bending method [*Um and Thurber*, 1983]. In our code, the rays are approximated using special basic functions. They follow along the topography

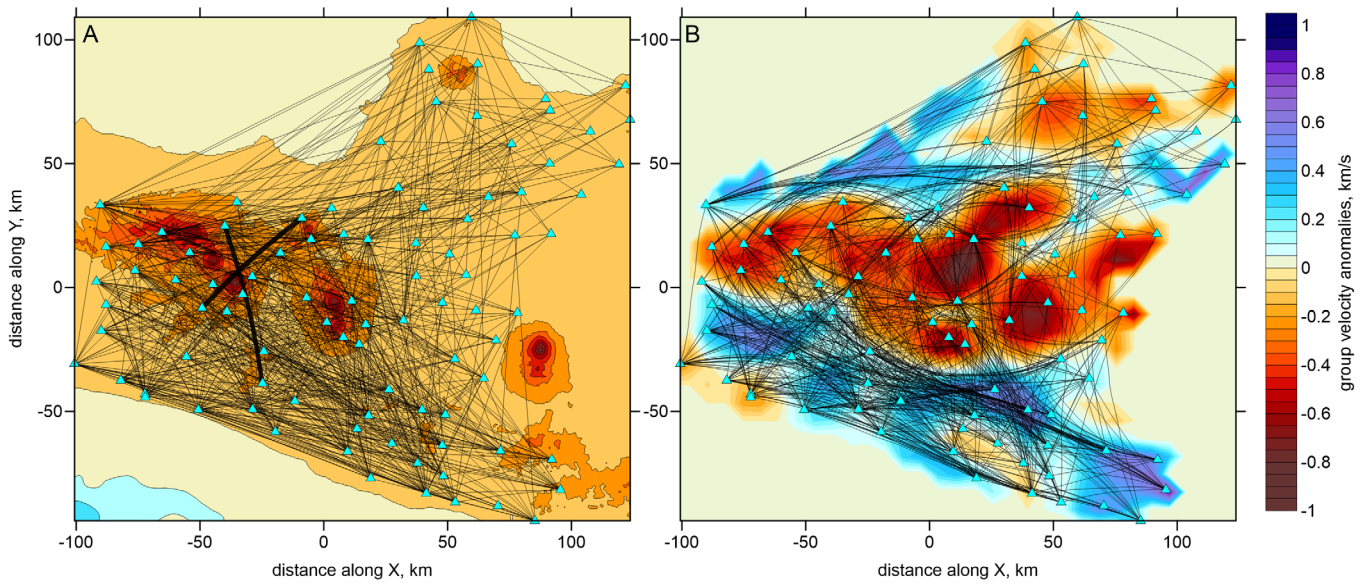

Figure 4. Example of the ray distributions for the data corresponding to the period of 7 s. (a) Thin lines depict the ray paths corresponding to the starting constant velocity and blue triangles depict the seismic stations. Two rays highlighted with thick lines demonstrate curving due to the topography features. Background is the topography. (b) Ray paths for the same data set after three iterations of inversions. The resulting anomalies of group velocities for the period of 7 s are presented in background. Blue triangles are seismic stations.

surface, which appears to be important in volcanic areas, where sharp topography features may behave as low-velocity anomalies. In the first iteration, we use a starting velocity computed as average of group velocities for all rays for a current frequency presented in Table 1. In next iterations, the rays were constructed taking into account the updated 2-D velocity model and relief.

Searching for a curve with minimum time is performed by subsequent deforming the ray path using four template functions presented in Figure 5, in which the deviation d can be approximated as:

$$d = A\ \sin(\pi\ s) \tag{1}$$

$$d = A\ [\cos(2\pi\ (s-0.5))+1]/2 \tag{2}$$

$$d = A\ [0.7375\ (\sin(3\pi\ s/2)+s] \tag{3}$$

$$d = A\ [0.7375\ (-\cos(3\pi\ s/2)+1-s] \tag{4}$$

where s is a normalized length along the current segment of the ray changing from 0 to 1, and A is the value of maximum deviation.

We start deforming the ray path from a straight line using the function (1). By varying the value of A, we determine the value that provide the minimum travel time. Then we divide the obtained curve in two equal parts. The first and second segments are bent using formulas (3) and (4), respectively. Then the ray is iteratively divided in three, four, five and more parts. For all inner parts, we implement the function (2), while for the first and the last segments, we use the functions (3) and (4), respectively. In each case, we vary the values of the A-parameter in formulas (1) to (4) in sufficiently large ranges

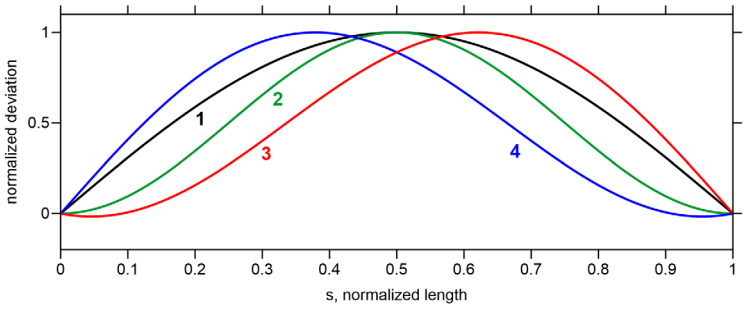

Figure 5. Four types of templates used for bending of the rays corresponding to formulas (1) to (4) in the text.

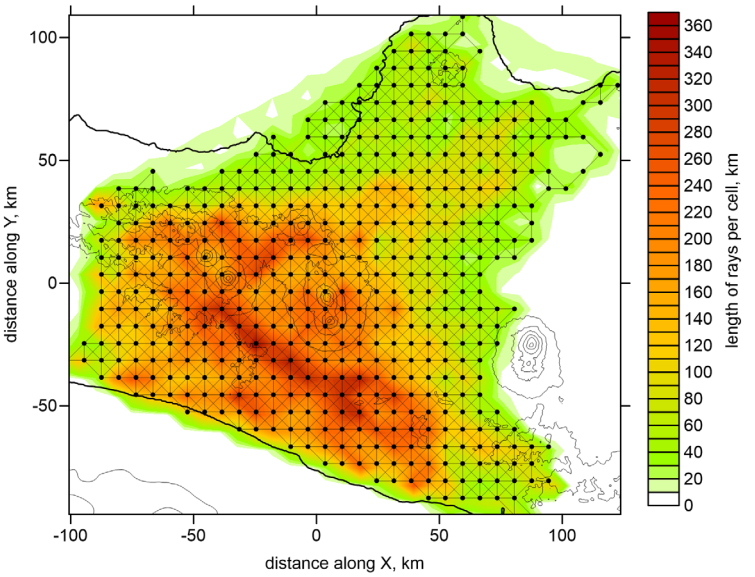

Figure 6. Example of ray density and grid nodes of the parameterization grid. Grey lines indicate the links between nodes used for flattening the model during the inversion. Topography is shown by contour lines.

to achieve the global minimum of travel time along the derived curve. The division of the ray stops when the segment length becomes less than a predefined value. This parameterization allows varying the angles of the ray in the starting and ending points and keeping continuous derivatives along the ray path. Figure 5 presents the ray paths for the period of 7 s for the cases of the 1st iteration (constant velocity and topography) and in the heterogeneous group velocity model derived after 5rd iteration.

The advantage of this method of forward modeling in respect to existing methods, such as ones based on the eikonal solutions used in some studies [e.g., *Lin et al.*, 2009] is that it is very fast and it provides the ray paths which directly used for computing the first derivative matrix.

The velocity data were parameterized with a set of nodes distributed across the area with ray density exceeding 10% of the average value (Figure 6). Between the nodes, the velocity was set using bi-linear interpolation. In our case, the grid spacing in areas with sufficient ray coverage was equal to 7 km. To avoid any artifacts related to grid orientation, we performed the inversions for several different orientations (namely, 0, 22, 45 and 66 degrees), and then averaged the results.

We inverted for the group-velocity deviations dU_j using the time residuals dt_i computed with respect to average group velocities indicated in Table 1 using a system of linear equations:

$$M_{ij}\ dU_j = \ dt_i \tag{5}$$

where M_{ij} is the first derivative matrix indicating the time variation of the i-th ray based on the unit group-velocity variation in the j-th node. The matrix is computed numerically along each ray path as:

$$M_{ij} = \int_{i-ray} -\frac{\Delta U(s)_{ij} ds}{V_0^2} \tag{6}$$

where $\Delta U(s)_{ij}$ is deviation of velocity at s-th point of the i-th ray path due to unit variation in the j-th node. It has a nonzero value only if the ray passes in the vicinity of the j-th node. In this case, $\Delta U(s)_{ij}$ is computed using the bi-linear interpolation presuming zero deviations in all nodes except for the j-th node, where the deviation is equal to 1.

The solution of the linear equation system was based on the LSQR algorithm [*Paige and Saunders*; 1982; *Nolet*, 1987]. To stabilize the solution, we used two additional damping blocks in the matrix. The first block, which controls the amplitude of the derived deviation, is diagonal and corresponds to equations with a single unknown parameter:

$$W^{am}\ dU_i = \ 0. \tag{7}$$

Increasing the weight W^{am} decreases the amplitude of the resulting group velocity deviations.

The second matrix block has a flattening effect upon the resulting anomalies. For each pair of neighboring nodes (indicated in Figure 6 with gray lines), we compose an equation:

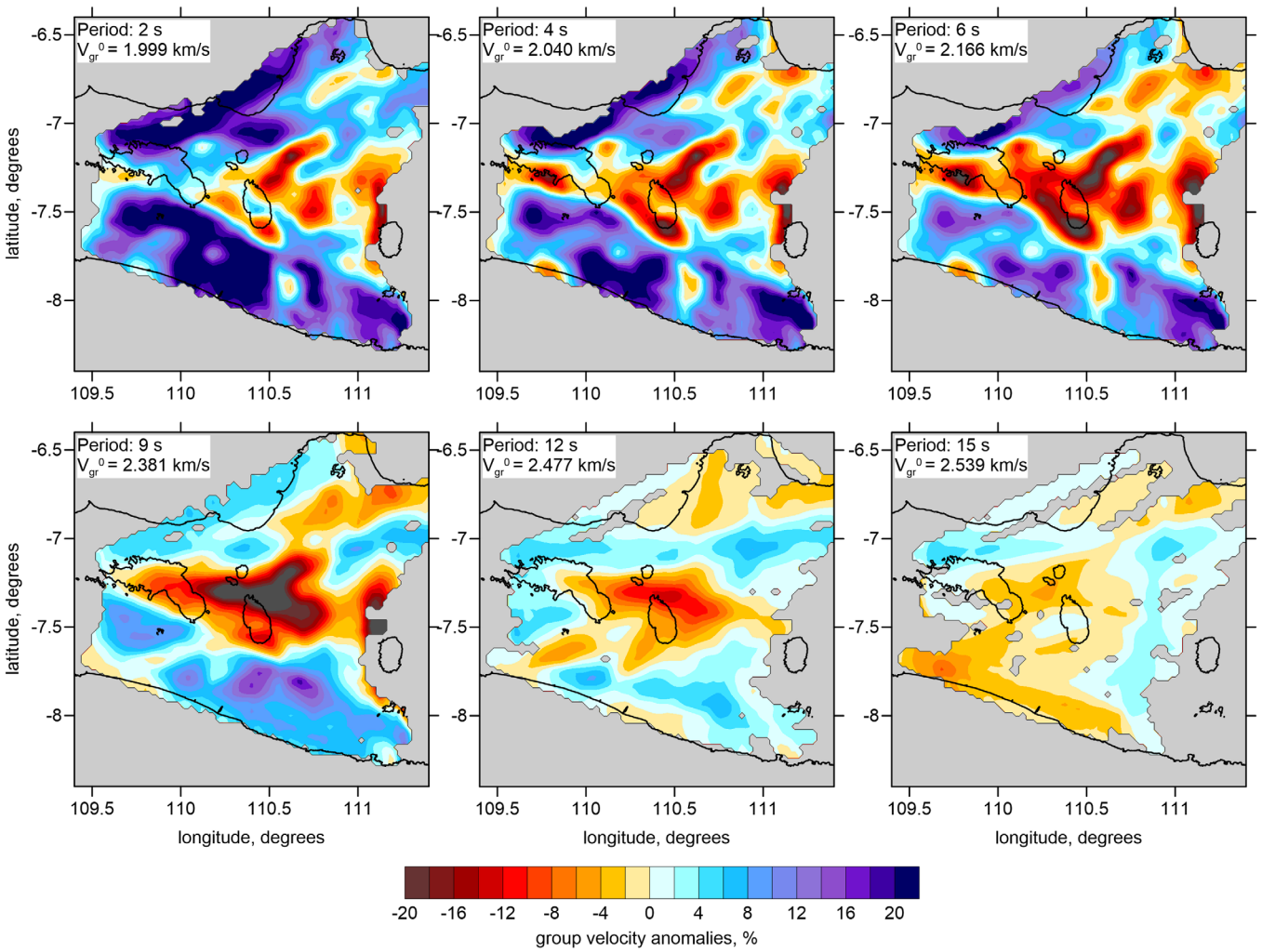

Figure 7. Examples of the two-dimensional maps of group velocities deviations for different periods indicated in the top-left corners of each plots. An average group velocity for each period used as reference values are indicated.

$$W^{sm}(dU_k - dU_m) = 0 \quad (8)$$

where U_k and U_m are the velocity anomalies for the neighboring nodes k and m. Increasing the weight W^{sm} makes the solution smoother. The values of the amplitude and flattening coefficients were set according to the results of several synthetic modeling trials, which are described below.

After performing the inversions for four grids and creating an average 2-D model, we use it for the next iteration, which includes the ray tracing, matrix calculation and inversion. The grid geometry remains unchanged: the velocity anomalies in each iteration are updated in the same nodes. In total, we performed three iterations. We fixed this number and played with the damping and smoothing parameters to derive the optimal solutions. The values of these parameters were estimated based on synthetic modeling. Having known values of synthetic anomalies, we were able to derive the optimal values of the inversion parameters to achieve the best similarity between the recovered and initial anomalies.

Examples of the derived two-dimensional group-velocity maps for different frequencies are presented in Figure 7. It is apparent that the major low-velocity area identified through this method is located between Merapi and Lawu in the same locations as was previously determined based on body-wave tomography. For the lowest frequency of 15 s and the correspondingly deepest wave propagation, this anomaly appears to be shifted southward. However, because this model is based on only 29 rays, this finding should be considered with discretion.

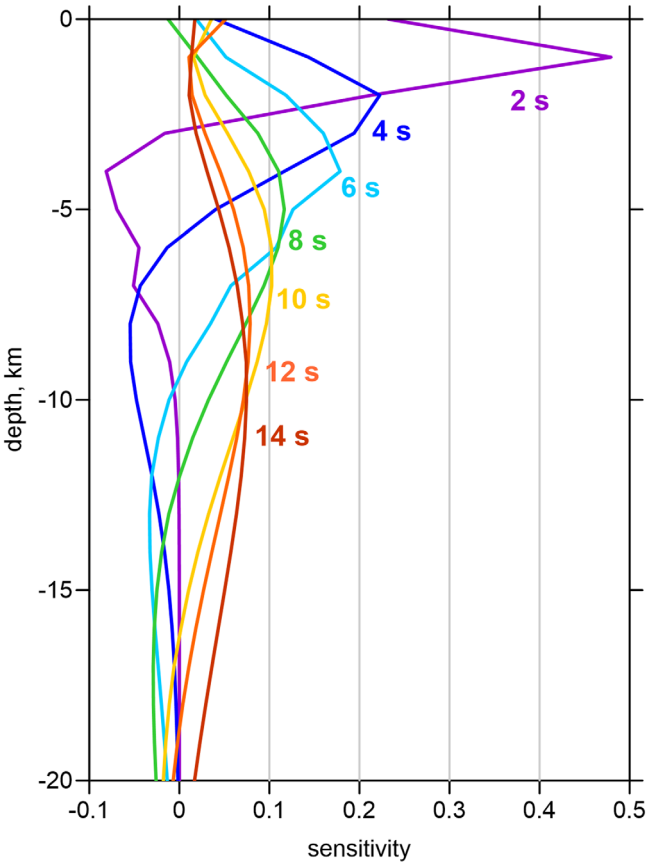

Figure 8. Examples of the Rayleigh wave sensitivity kernels for several selected periods indicated with different colors.

4.2. Three-Dimensional Tomography for the S-Wave Velocities

Group velocities actually depend on several parameters: the seismic velocities *Vp*, *Vs*, density ρ and quality factor *Q*. However, the fundamental mode of the Raleigh wave is most sensitive to the distribution of shear velocity. Therefore, for our calculations, we fixed ρ and *Q* according to an a-priori 1D reference model and evaluated for the variations in *Vs* that enabled the best fit with the observed group velocities. The *P*-velocity was updated according to the derived *S*-velocity using a constant *Vp/Vs* ratio equal to 1.75.

After generating a series of maps of group velocities for the entire range of frequencies, instead of considering the inter-station dispersion curve, we analyzed the dispersion curves for every point of the study area. The problem of determining the 3-D distribution was thus reduced to the conversion of dispersion curves (*U(f)*) to the one-dimensional distribution of *Vs(z)* at each point of the study area. To solve this problem, we used an iterative method of perturbations. The forward modeling (i.e., the calculation of group velocities in the 1D velocity model) was performed using algorithms developed by *Herrmann* [1987]. At each iteration, we presume a linear relationship between small variations in velocity variations *dV* at some depth (in *i*-th layer) and the group-velocity deviation *dU* at *j*-th frequency:

$$dU_j = M_{ij}^{3D} dV_i \tag{9}$$

where $M_{ij}^{3D} = \frac{\partial U_j}{\partial V_i}$ is the first derivative matrix representing the sensitivity kernel. To obtain this matrix, we calculated the group velocities for an initial model and for a model with a perturbed velocity at the *i*-th depth level, and then took the difference between the derived group velocities at the *j*-th frequency. In our case, we used a value of perturbation of 0.01 km/s and a depth increment of 1 km. Examples of sensitivity kernels for several frequencies are shown in Figure 8. It is shown that for higher frequencies (i.e., shorter periods), higher sensitivity is achieved at shallower depths, whereas the lower frequency kernels are more sensitive to deeper structures.

Using equation (9) for the case of the 1D inversion, we constructed a number of linear equations equal to the number of discrete frequencies (14 in this case). The number of unknowns is equal to the number of depth layers. We used increments of 1 km from depths of zero to 25 km; therefore, in total, there were 25 unknowns. To resolve the problem of underdetermination, we linked the parameters with additional equations that damp the gradients between the depth levels:

$$W^{ver}(dU_k - dU_{k+1}) = 0 \tag{10}$$

where U_k and U_{k+1} are the velocity anomalies for the neighboring depth levels *k* and *k+1*. Increasing the weight W^{ver} makes the vertical velocity variations smoother. The obtained system of linear equations is

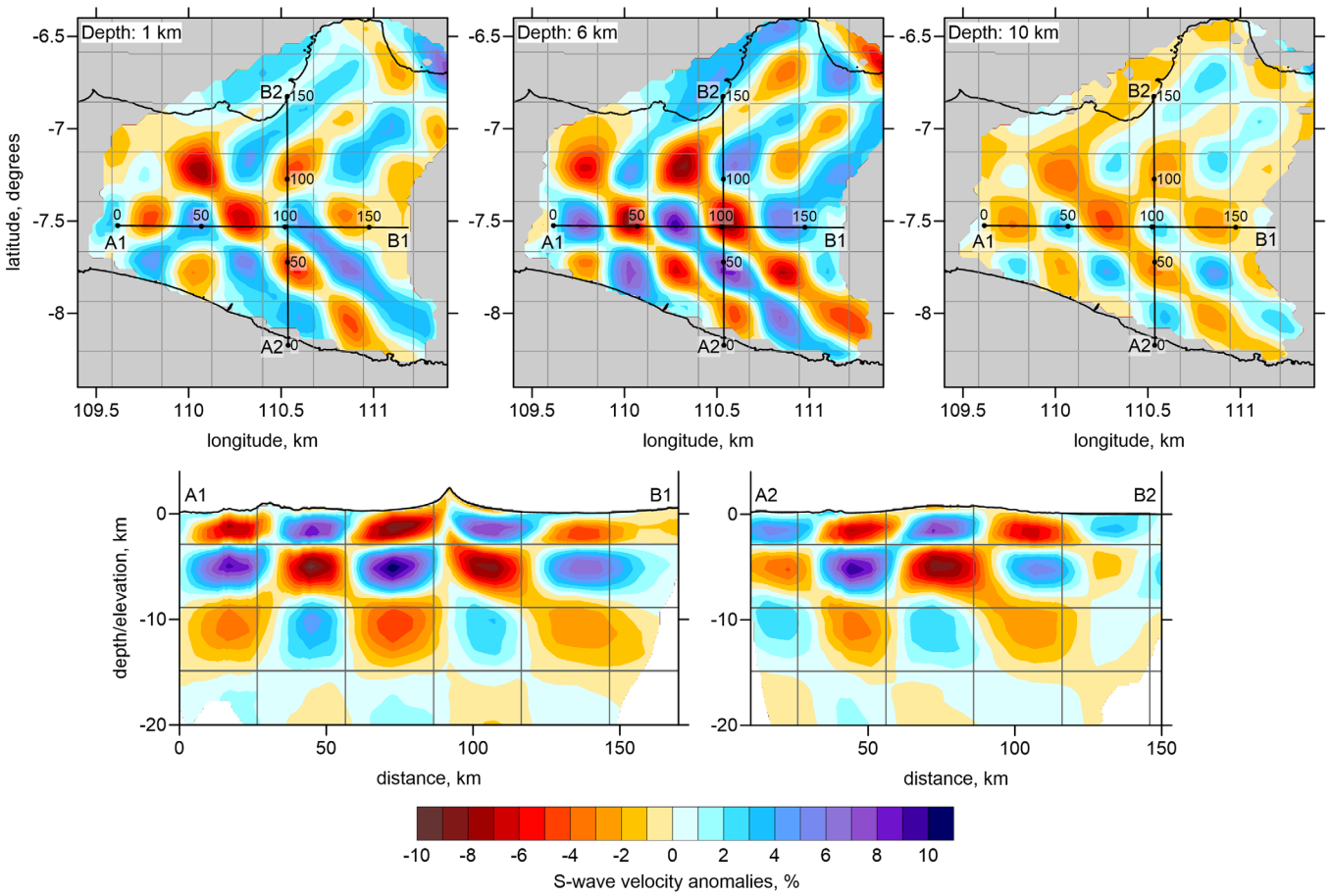

Figure 9. Checkerboard test. Upper row shows the recovering result in three horizontal sections. Lower row present the recovering result in two vertical sections with the locations shown in the upper maps. In both cases of horizontal and vertical sections, the gray lines indicate the locations of the true synthetic anomalies.

solved using the LSQR algorithm [*Nolet*, 1987]. After determining the 1D velocity distribution, we used it to calculate new sensitivity kernels and perform the inversion again. When a stable, nonchanging solution for the velocity model is achieved, the iterations are stopped.

Using this algorithm, we first estimated an optimal 1D velocity model for the entire study area using an average dispersion curve. We then used this model as the reference model for 3-D inversion.

For the 3-D inversion, we calculated the dispersion curves for every point of the study area using the group-velocity maps (Figure 7) determined in the 2-D inversion step. For each point that coincided with nodes used for the 2-D tomography, we calculated the difference between the modeled dispersion curve and the observed curve. For each node, we computed the sensitivity kernels corresponding to the current 1D velocity model at every point. At the initial step, we used the 1D velocity model for the entire region, but in the following iterations, the velocity distribution at each node differentiates according to the derived 3-D model. We performed this inversion simultaneously for all nodes of the grid. During the inversion, we damped the gradients both laterally (for the pairs indicated with gray lines in Figure 6) and vertically using equations (8) and (10). We also used amplitude damping by adding a diagonal matrix according to equation (7).

After performing the inversion, we obtained the 3-D distribution of the velocity anomalies. These were added to the reference model and used to calculate new sensitivity kernels and compose a new system of linear equations. This iterative procedure is typically repeated several times (three times, in our case).

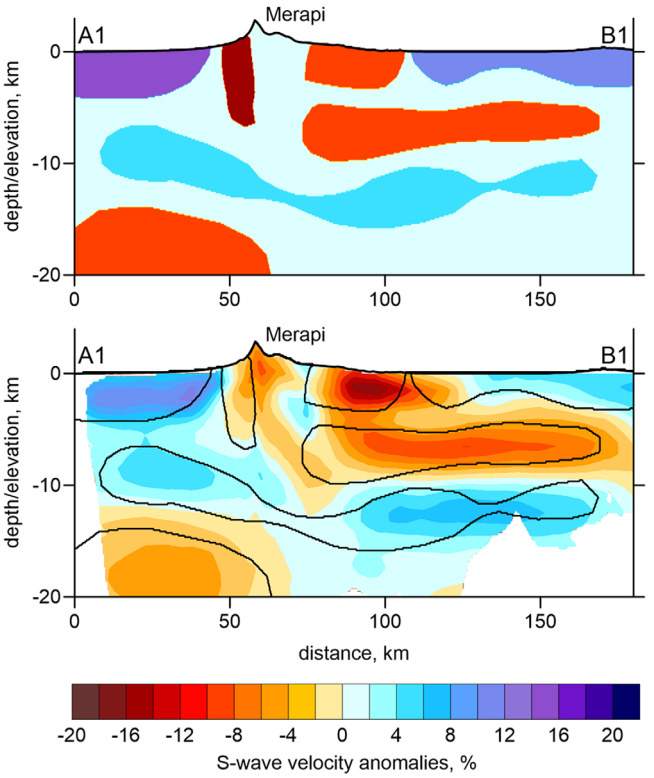

Figure 10. Synthetic test with free-shaped anomalies defined in vertical section A1-B1 (See the location in Figure 11). (top) The original synthetic anomalies; (bottom) the recovering result. Think contours highlight the shapes of the original anomalies. The topography along the section is given for the reference.

5. Synthetic Modeling

To assess the spatial resolution of the derived seismic model, we performed a series of synthetic tests. The synthetic model was composed of an absolute one-dimensional model (including *Vp*, *Vs*, and ρ) with overlapping three dimensional anomalies. The anomalies are defined similarly as in the LOTOS code by *Koulakov* [2009] using several different options, such as checkerboard and free-shaped polygonal patterns defined in horizontal or vertical sections. In our case, we only considered the 3-D perturbations of *Vs*, whereas *Vp* and ρ were modeled one-dimensionally.

The first stage in creating the synthetic data is generation of the two-dimensional maps of group velocities for all frequencies in the experimental data set. For each point within the study area, we solved a forward problem of computing the group Rayleigh wave velocity based on the 1D model corresponding to that point with perturbed *Vs* and unperturbed *Vp* and ρ [*Herrmann*, 1987]. At this stage, the 1D distributions of velocities and density used for computing the group velocity were calculated in respect to the topography elevation.

In the second stage, we computed the travel times and apparent group velocities for all frequencies and for all available pairs of stations in the original data set. The files generated in this step have the identical format as the initial experimental data files used as inputs for the inversion. Then, the parameters of the "true" velocity model were "forgotten," and we recovered the model using the same procedure followed for the experimental data. As a result, we first obtained 2-D maps of group velocities, and then inverted them to three-dimensional distribution of S-wave velocity.

Here, we present the results of two synthetic tests. The first test consists of the recovery of the checkerboard model with periodic anomalies with amplitudes of $\pm$ 7%. The horizontal size of these anomalies is 30 km; in the vertical direction, the signs change at depths of 3 km and 13 km. The recovery results are shown in Figure 9 in three horizontal and two vertical sections. We observe that in the central part of the model, the anomalies in all three layers are correctly restored. In the southern and easternmost parts of the study area, there is some leakage of the amplitudes and diagonal smearing; however, the major patterns are recovered at the right depths. In the vertical sections, we note that three layers with different signs of anomalies are correctly recovered.

The second test illustrated in Figure 10 represents a realistic situation observed following the inversion of experimental data. The synthetic anomalies are defined along a vertical section passing through Merapi, which are shown in Figure 11. The anomalies are defined as polygonal prisms with thicknesses of 50 km in the direction perpendicular to the section. This test shows that with the existing data, we are able to resolve three closely located negative anomalies beneath Merapi. The shallow positive anomalies in the forearc and backarc are robustly resolved in our model. The deep anomaly below 15 km depth is also resolved, although its intensity and depth are reduced. Both of these tests demonstrate that the anomalies identified

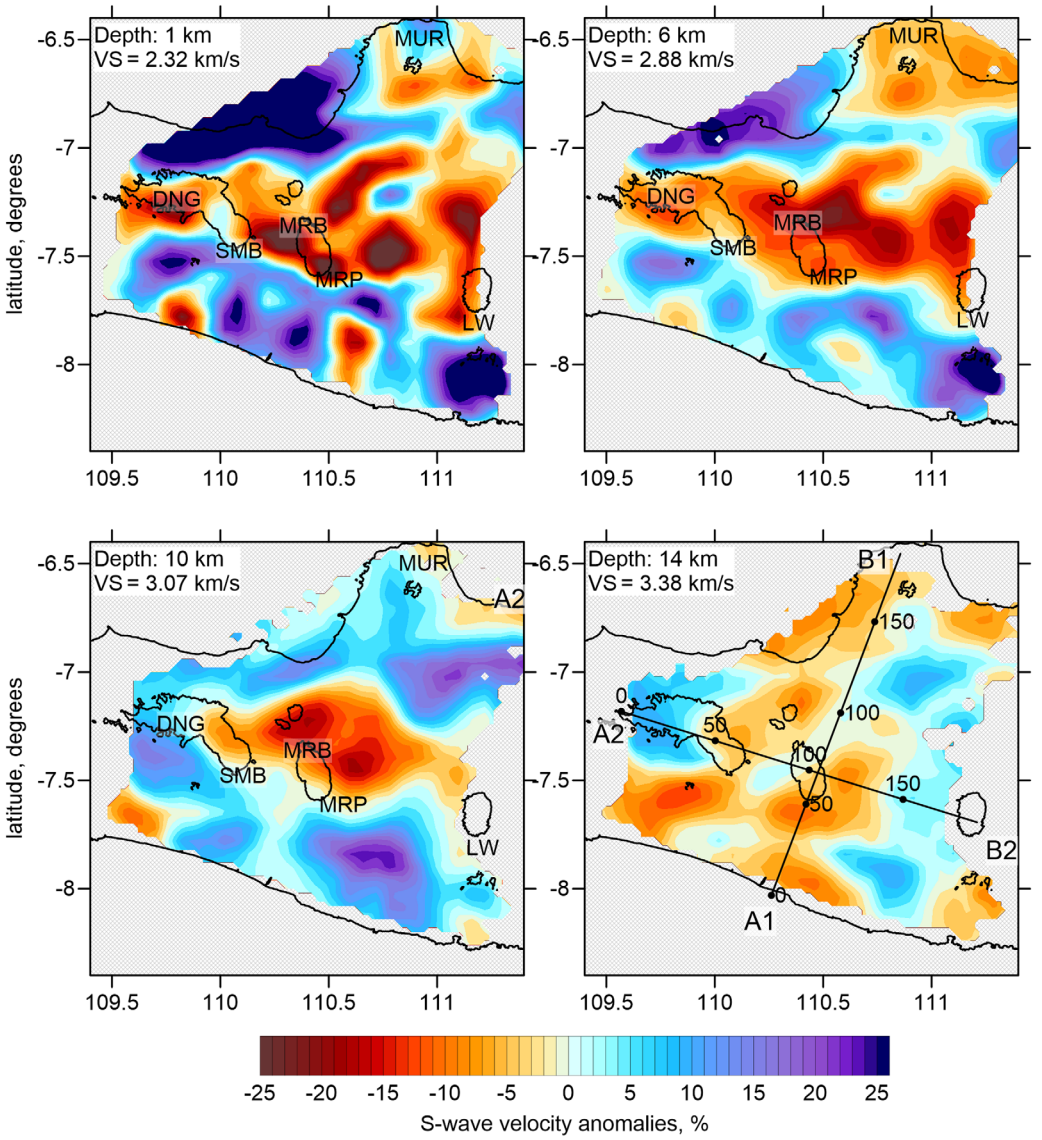

Figure 11. Anomalies of the S-wave velocity model in horizontal sections. The reference velocity values and depths of the sections are indicated in the top-left corners of the plots. The contour line of topography at 1000 m altitude are shown with black lines. The main volcanoes are indicated as: DNG–Ding, SMB–Sambung, MRB–Merbabu, MRP–Merapi, MUR–Muria and LW–Lawu. The locations of two vertical sections are shown in the section of 14 km.

using the experimental data can be robustly recovered using the existing data. However, there is some amplitude leakage that must be considered in interpretation of the results of observed data inversion.

6. Inversion Results and Discussion

The main result of the tomographic inversion is the 3-D distribution of the S-velocity beneath the Central Java derived from the analysis of ambient noise data. The derived 1D distributions in each point of the study area are taken in respect to the corresponding topography altitude. We present the deviations of the S-velocity with respect to the average model in four horizontal sections in Figure 11 and in two vertical sections in Figure 12. In addition, in Figure 12, we present the distribution of absolute velocity in the same sections. In general, we observe strong variations in the S-wave velocity, especially at shallow depths. Indeed, in the area between the coast and the volcanoes, our findings reveal a strong high-velocity anomaly with an amplitude that exceeds 25%. Beneath and to the south of Merapi, we observe strong negative anomalies with amplitudes that reach −25%. Therefore, the variations presented herein are of the same order of

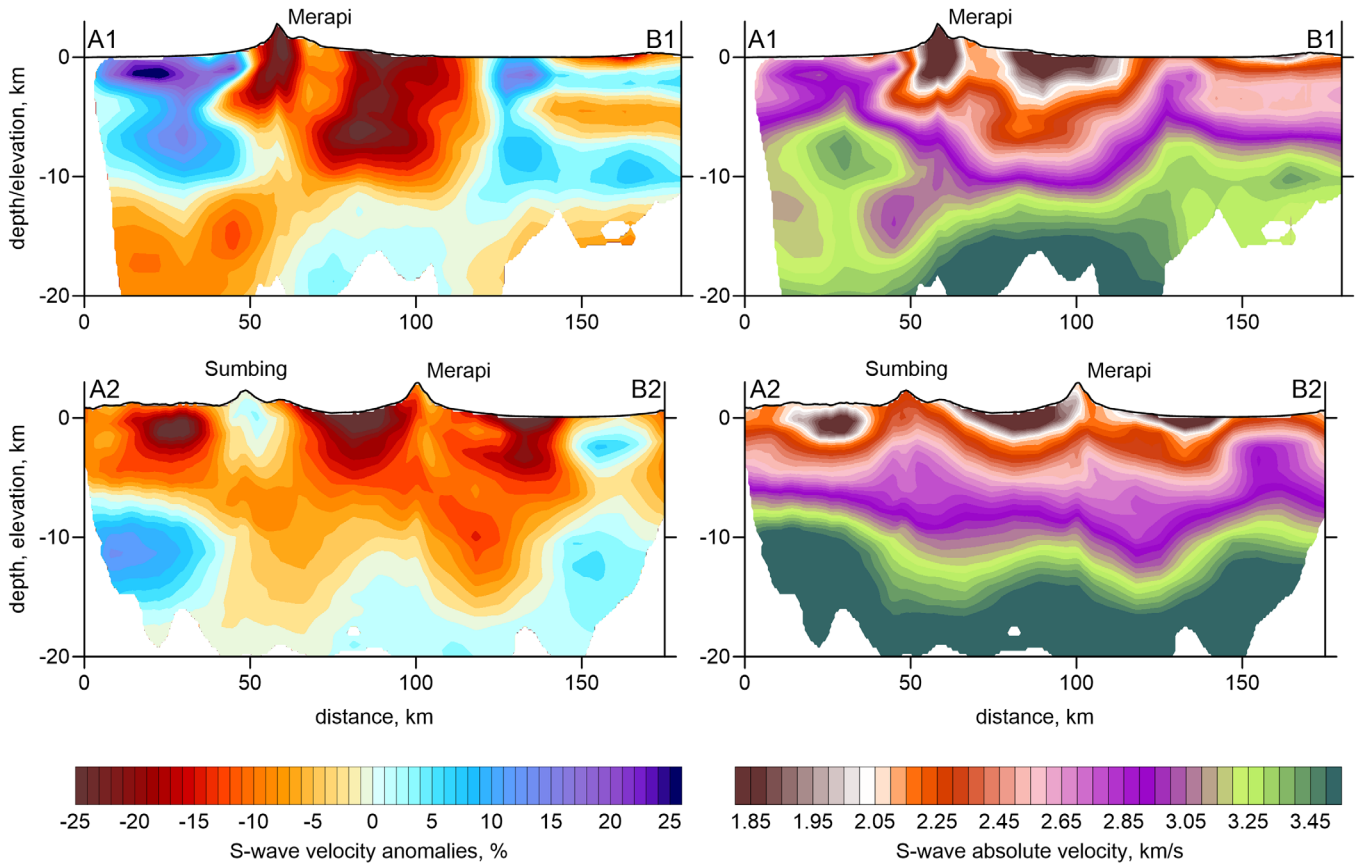

Figure 12. Resulting S-wave model in two vertical sections with the locations indicated in Figure 11. Left column present the anomalies, and the right column shows the absolute velocity distributions. The vertical scale is three time exaggerated. The exaggerated topography along the profiles is presented above each plot.

magnitude as those reported in previous tomographic studies based on travel-time tomography [*Koulakov et al.*, 2007, 2009].

In Figure 13, we compare the results of ambient noise tomography (ANT) calculated in this study with the results of the model derived from the local earthquake travel-time tomography (LET) [*Koulakov et al.*, 2009]. We present *S*-velocity anomalies for the same depth of 5 km and in almost the same vertical section passing through Merapi. In the horizontal section (Figures 13a and 13c), we see that the main features, such as the high-velocity forearc and low-velocity anomalies between volcanoes, appear similar in both models. However, there are differences in the details. For example, in the LET results, the most prominent low-velocity anomaly has a high magnitude across the entire area between Merapi and Lawu, whereas in the ANT model, the eastern part of the anomaly in the vicinity of Lawu appears to be less significant. This difference can be partially explained by the lower resolution of the ANT model in the eastern area, as well as by some leakage of the amplitude of anomalies, as was noted from the results of the checkerboard test (Figure 9). We must also note the significant vertical smearing of the LET results, which suggest that some differences between the models' results may be caused by projection of anomalies from other depths in this model.

For the vertical section (Figures 13b and 13d), we also observe an overall good fit of the main anomalies detected in both the LET and ANT models. The most prominent feature, the strong low-velocity anomaly beneath the northern flank of Merapi, is observed in both models, although it appears deeper in the LET model. In the ANT model, an anomaly beneath the Merapi cone is apparent, whereas in the LET model, this anomaly is not revealed, most likely because of insufficient data coverage. Interestingly, a large anomaly at the bottom-left corner of the ANT section seems to be consistent with the inclined low-velocity anomaly in the LET model that links the volcano-related structures with the subducting slab. We also observe a general correlation of the shallow anomalies in the area to the south of Muria, but again, the depth ranges of the

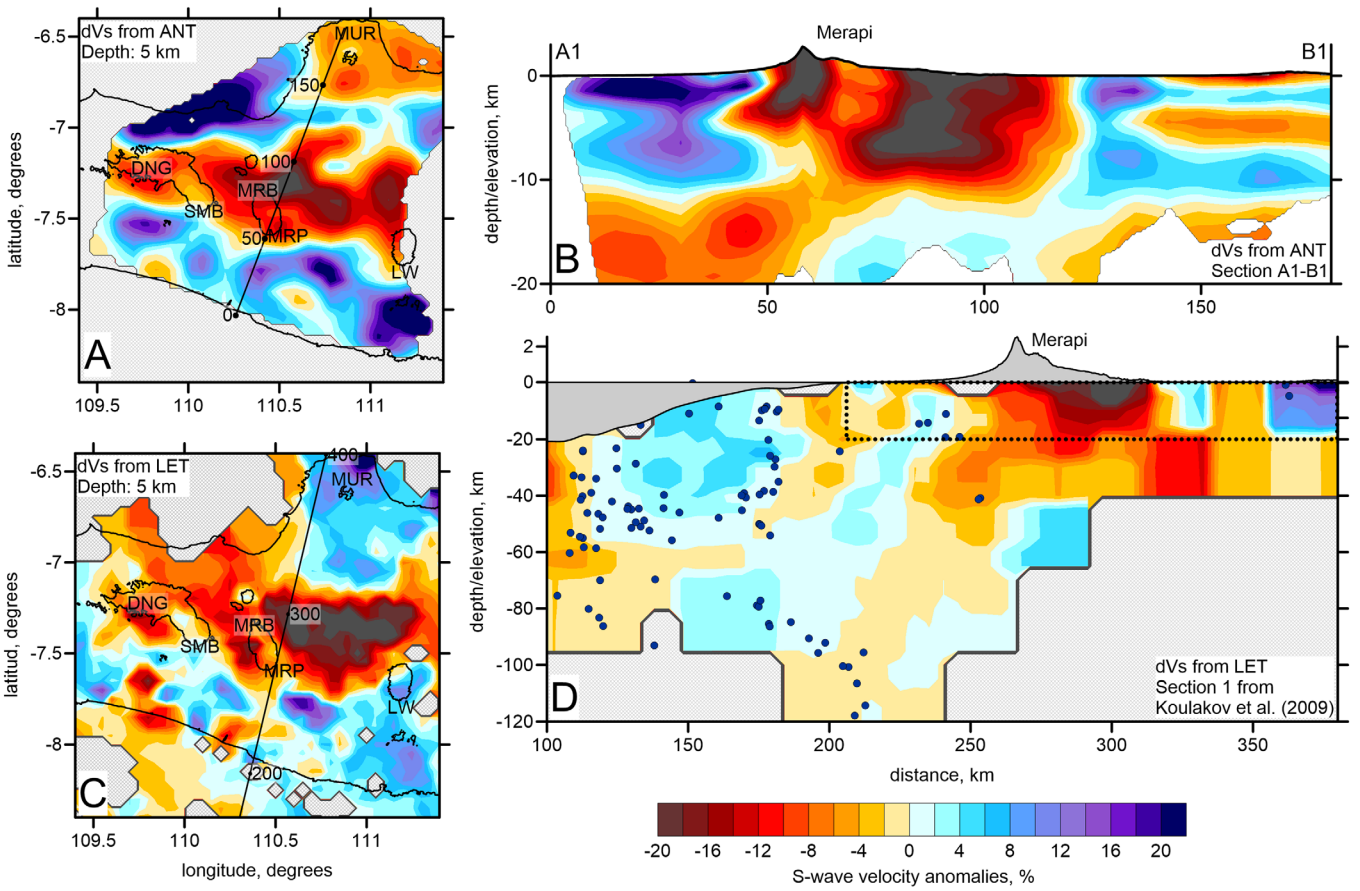

Figure 13. Comparison of the ambient noise tomography (ANT, this study) with the body wave local earthquake tomography model [LET, *Koulakov et al.*, 2014]. (a and c) Horizontal sections at 5 km of the ANT and LET models. The contour line of topography at 1000 m altitude are shown with black lines. (b and d) The vertical sections of the ANT and LET models along the profiles indicated in Figures 13a and 13c. In Figure 13b, the vertical scale is twice exaggerated. Blue points in Figure 13d show the earthquakes. Dotted line in Figure 13d depicts the area corresponding to the section in Figure 13b. The exaggerated topography along the profiles is presented in Figures 13b and 13d.

retrieved anomalies are different. Based on comparison of these results, and taking into consideration the results of synthetic tests for both cases, we conclude that the ANT model has superior resolution to the depth of 20 km. Therefore, it provides important complementary information that advances discussion of the structure of the plumbing system beneath Merapi and surrounding volcanoes.

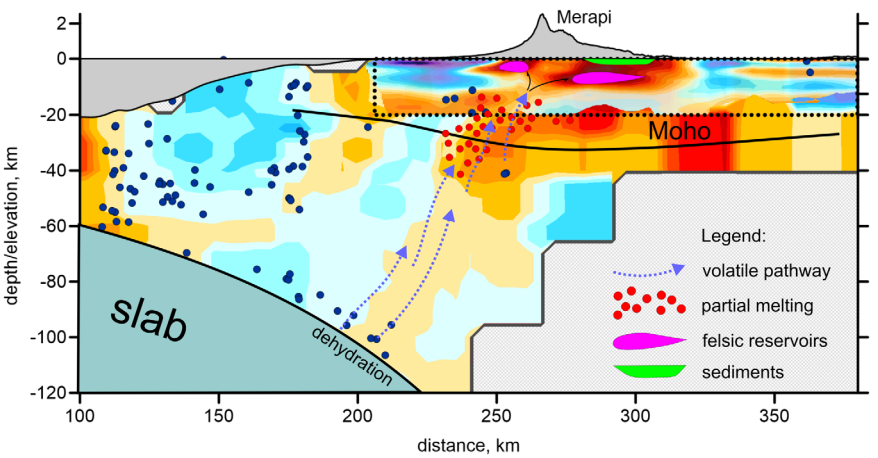

Figure 14. Overlapped results of the LET and ANT in the vertical section (same as in Figure 13d) and possible interpretation. Exaggerated topography is shown above the plot. The Moho interface is schematically indicated according to [*Wölbern and Rümpker*, 2016]. Blue dots are the earthquakes. The gray area depicts the subducting slab. The other symbols are explained in the legend.

According to the results of the ANT model, the large low-velocity anomaly beneath the northern flank of Merapi (section A1–B1, Figure 12) seems to be separated into two parts. The synthetic test with realistic anomalies in Figure 10 has indicated that in the ANT model, we can robustly resolve this fine variation by depth. We propose that the upper portion of this anomaly represents a thick layer of pyroclastic sediments accumulated over the long eruptive history of Merapi. Based on our model, the thickness of this layer may be larger than 1 km. The strong low-velocity anomaly between depths of 4 km and 8 km located beneath this sedimentary layer may be associated with a large, shallow felsic magma reservoir, as was proposed previously based on the results of the LET model by *Koulakov et al*. [2009]. The same work clearly demonstrated horizontally oriented anisotropy in this layer that may indicate a sill structure of this reservoir. A similar sill structure for a felsic magma reservoir at approximately the same range of depth was identified beneath the Toba Caldera of Sumatra [*Jaxybulatov et al*., 2014]. We speculate that this reservoir may accumulate magma from deeper sources and deliver it to the surrounding volcanoes. In section A2–B2, we see that this anomaly is present beneath all volcanoes along the profile (Sumbing–Merapi–Lawu). It is notable that in this section, the edifices of the volcanoes are mostly associated with higher velocities at the shallowest depths, whereas in areas between the volcanoes, the shallow anomalies are generally negative. We hypothesize that the high-velocity anomalies beneath these volcanoes may represent the rigid properties of the volcano edifices, which are composed of highly consolidated igneous rock. In areas between the volcanoes, the shallow structures are mainly associated with volcanoclastic deposits that are usually associated with low-velocity anomalies.

A new finding of this study is a clear low-velocity anomaly beneath Merapi at depths as low as 8 km that may represent the active magma reservoir. This interpretation appears to be consistent with the occurrence of volcano-tectonic events beneath Merapi in the same range of depth [*Ratdomopurbo and Poupinet*, 1995, 2000; *Beauducel et al*., 2000].

The low-velocity anomaly at the bottom-left corner of the results of the ANT model in the vertical section A1–B1 (Figure 13b) may represent the top of the inclined "root" that was identified with the LET model. Taking into consideration the results of the checkerboard test in Figure 8, there is some uncertainty associated with the depth of this anomaly; however, it is notable that it seems to be clearly separated from the crustal anomalies. The ANT model appears to have a tendency to shift the deep boundaries higher; consequently, the real location of this anomaly may be deeper than is indicated by these results. The critical implication is that by using the ANT model, we were able to separate different levels of anomalies that were smeared and indistinguishable in the LET results.

Based on the results of this study, we can reevaluate the scenario proposed in previous tomography papers about Merapi. A schematic cartoon illustrating the processes taking place beneath Central Java is shown in Figure 14. As was proposed by *Luehr et al*. [2013], the magma sources beneath Central Java are inferred to have originated in the subducting slab at ~100 km depth. We observe an increased level of slab-related seismicity at this depth that may represent the process of dehydration and the resulting release of volatiles [*Peacock*, 1990; *Maruyama and Okamoto*, 2007]. When these volatiles pass through the mantle wedge, they react with the mantle rocks and lower their melting temperature [*Poli and Schmidt*, 1995]. Therefore, at the base of the crust, which is at a depth of approximately 38 km [*Wölbern and Rümpker*, 2016], there may be a large amount of partially molten rocks and volatiles. As proposed by *Koulakov and Shapiro* [2015], the continental crust may become a barrier for basal magmas from the mantle. Magma diapirs may ascend through the lower mafic crust, but they cannot penetrate further into the upper felsic crust because of insufficient buoyancy. The low-velocity anomaly at a depth of ~20 km in our model may represent the top of the basic magma pathway at a boundary between the lower and upper crust. We observe that this anomaly is clearly separated from anomalies in the upper crust. Meanwhile, the overheated volatiles may continue to ascend. They bring substantial heat from the mantle wedge and may cause melting of felsic rock in the upper crust. These partially molten materials are inferred to form a complex system of reservoirs at depths between 8 and 4 km that feed several volcanoes in Central Java.

7. Conclusions

For this study, based on the analysis of ambient noise data recorded in 2004 by more than 100 seismic stations within the MERAMEX Project, we developed a model of S-wave velocity in the upper crust beneath

Central Java. We have applied a new algorithm for ambient noise tomography that is based on iterative linearized inversion. Some components implemented in this software, such as parameterization and damping, were successfully tested previously in body-wave tomography algorithm [e.g., LOTOS, *Koulakov*, 2009].

Using synthetic tests, we have demonstrated the high resolution enabled by the available data. With ambient noise tomography in particular, finer velocity variations in the vertical direction can be resolved compared with body-wave tomography.

The features indicated by the results of this study are generally consistent with previous models derived from local earthquake travel-time tomography. In both models, we observe a large low-velocity anomaly located beneath the Merapi and Lawu volcanoes. In this study, we have demonstrated that this upper-crustal anomaly is separate from the deeper anomaly that connects the volcanic area with the subducting slab at 100 km depth. Furthermore, within this anomaly, we can differentiate two layers. The shallower layer, down to ~1 km depth, may represent the pyroclastic sediments accumulated on the flanks of Merapi over its eruptive history. The deeper anomaly, located at depths of 4–8 km, may be associated with a large felsic magma reservoir that feeds the surrounding volcanoes.

A new finding of this study is a clear low-velocity anomaly beneath the summit of Merapi reaching as low as 8 km in depth. This finding fits with the distribution of the volcano-tectonic seismicity, and may represent the active magma chamber that is responsible for the present volcanic activity of Merapi.

Acknowledgments

We are grateful for rigorous reviews by Anatoly Levshin, Antonio Villasegnor and an anonymous reviewer that helped us to make considerable corrections in the algorithm and improve the paper. Work by IK was supported by the Russian Scientific Foundation (grant #14-17-00430). The contribution of EK was supported by the grant of Russian Foundation of Basic Researches (#16-35-00099), and the work of NS and KJ was supported by the French project 'Labex UnivEarth' and by the Université Sorbonne Paris Cité via the project 'VolcanoDynamics'. The authors extend their appreciation to the Deanship of Scientific Research at King Saud University for funding this study through the International Research Group project IRG14-21. All the results of this study can be reproduced by anyone using the full version of the algorithm together with experimental data files that can be downloaded from www.ivan-art.com/science/surf_nonlin_java.zip. The brief manual how to run the code is included.

References

Beauducel, F., F. H. Cornet, E. Suhanto, T. Duquesnoy, and M. Kasser (2000), Constraints on magma flux from displacements data at Merapi volcano, Java, Indonesia, *J. Geophys. Res.*, *105*, 8193–8203.

Bensen, G. D., M. H. Ritzwoller, M. P. Barmin, A. L. Levshin, F. Lin, M. P. Moschetti, N. M. Shapiro, and Y. Yang (2007), Processing seismic ambient noise data to obtain reliable broad-band surface wave dispersion measurements, *Geophys. J. Int.*, *169*(3), 1239–1260, doi: 10.1111/j.1365-246X.2007.03374.x.

Bohm, M., C. Haberland, and G. Asch (2013), Imaging fluid-related subduction processes beneath Central Java (Indonesia) using seismic attenuation tomography, *Tectonophysics*, *590*, 175–188.

Campillo, M., H. Sato, N. M. Shapiro, and R. D. Van Der Hilst (2011), New developments on imaging and monitoring with seismic noise, *C. R. Geosci.*, *343*(8-9), 487.

Fang, H., H. Yao, H. Zhang, Y. C. Huang, and R. D. van der Hilst (2015), Direct inversion of surface wave dispersion for three-dimensional shallow crustal structure based on ray tracing: Methodology and application, *Geophys. J. Int.*, *201*(3), 1251–1263.

Haberland, C., M. Bohm, and G. Asch (2014), Accretionary nature of the crust of Central and East Java (Indonesia) revealed by local earthquake travel-time tomography, *J. Asian Earth Sci.*, *96*, 287–295.

Herrmann, R. B. (1987), Computer programs in seismology, Saint Louis Univ., St. Louis, Mo. [Available at http://www.eas.slu.edu/People/RBHerrmann/CPS330.html.]

Jaxybulatov, K., N. M. Shapiro, I. Koulakov, A. Mordret, M. Landès, and C. Sens-Schönfelder (2014), A large magmatic sill complex beneath the Toba caldera. *Science*, *346*(6209), pp. 617–619, doi:10.1126/science.1258582.

Jousset, P., et al. (2012), The 2010 explosive eruption of Java's Merapi volcano—A '100-year'event, *J. Volcanol. Geotherm. Res.*, *241*, 121–135.

Koulakov, I. (2009), LOTOS code for local earthquake tomographic inversion. Benchmarks for testing tomographic algorithms, *Bull. Seismol. Soc. Am.*, *99*(1), 194–214, doi:10.1785/0120080013.

Koulakov, I., et al. (2007), *P* and *S* velocity structure of the crust and the upper mantle beneath central Java from local tomography inversion, *J. Geophys. Res.*, *112*, B08310, doi:10.1029/2006JB004712.

Koulakov, I., A. Jakovlev, and B. G. Luehr (2009), Anisotropic structure beneath central Java from local earthquake tomography, *Geochem. Geophys. Geosyst.*, *10*, Q02011, doi:10.1029/2008GC002109.

Levshin, A. L., T. B. Yanovskaya, A. V. Lander, B. G. Bukchin, M. P. Barmin, L. I. Ratnikova and E. N. Its (1989), Recording, identification, and measurement of surface wave parameters, in *Seismic Surface Waves in a Laterally Inhomogeneous Earth*, edited by V. I. Keilis Borok, pp. 131–182, Kluwer Acad., Dordrecht, Netherlands.

Lin, F. C., M. H. Ritzwoller, and R. Snieder (2009), Eikonal tomography: Surface wave tomography by phase front tracking across a regional broad-band seismic array, *Geophys. J. Int.*, *177*(3), 1091–1110.

Luehr, B. G., I. Koulakov, W. Rabbel, J. Zschau, A. Ratdomopurbo, K. S. Brotopuspito, P. Fauzi, and D. P. Sahara (2013), Fluid ascent and magma storage beneath Gunung Merapi revealed by multi-scale seismic imaging, *J. Volcanol. Geotherm. Res.*, *261*, 7–19.

Macquet, M., A. Paul, H. A. Pedersen, A. Villaseñor, S. Chevrot, M. Sylvander, D. Wolyniec, and Pyrope Working Group (2014), Ambient noise tomography of the Pyrenees and the surrounding regions: Inversion for a 3-D Vs model in the presence of a very heterogeneous crust, *Geophys. J. Int.*, *199*(1), 402–415.

Maruyama, S., and K. Okamoto (2007), Water transportation from the subducting slab into the mantle transition zone, *Gondwana Res.*, *11*(1), 148–165.

Nolet, G. (1987), Seismic wave propagation and seismic tomography, in *Seismic Tomography*, edited by G. Nolet, pp. 1–23, D. Reidel, Dordrecht, Netherlands.

Paige, C. C., and M. A. Saunders (1982), LSQR: An algorithm for sparse linear equations and sparse least squares, *ACM Trans. Math. Software*, *8*(1), 43–71.

Peacock, S. A. (1990), Fluid processes in subduction zones. *Science*, *248*(4953), 329–337.

Poli, S., and M. W. Schmidt (1995), H2O transport and release in subduction zones: Experimental constrains on basaltic and andesitic systems, *J. Geophys. Res.*, *100*, 22,299–22,314.

Ratdomopurbo, A. and G. Poupinet (1995), Monitoring a temporal change of seismic velocity in a volcano: Application to the 1992 eruption of Mt. Merapi (Indonesia), *Geophys. Res. Lett.*, *22*, 775–778.
Ratdomopurbo, A., and G. Poupinet (2000), An overview of the seismicity of Merapi volcano (Java, Indonesia), 1983–1994, *J. Volcanol. Geotherm. Res.*, *100*(1), 193–214.
Riedesel, M. A., R. D. Moore, and J. Orcutt (1990), Limits of sensitivity of inertial seismometers with velocity transducers and electronic amplifiers, *Bull. Seismol. Soc. Am.*, *80*, 1725–1752.
Ritzwoller, M. H., and A. L. Levshin (1998), Eurasian surface wave tomography: Group velocities, *J. Geophys. Res.*, *103*, 4839–4878, doi:10.1029/97JB02622.
Ritzwoller, M. H., F. C. Lin, and W. Shen (2011), Ambient noise tomography with a large seismic array, *C. R. Geosci.*, *343*, 558–570.
Shapiro, N. M., and M. Campillo (2004), Emergence of broadband Rayleigh waves from correlations of the ambient seismic noise, *Geophys. Res. Lett.*, *31*, L07614, doi:10.1029/2004GL019491.
Shapiro, N. M., and I. Y. Koulakov (2015), Probing the underbelly of a supervolcano, *Science*, *348*, 758–759, doi:10.1126/science.aab1828.
Shapiro, N. M., and M. H. Ritzwoller (2002), Monte-Carlo inversion for a global shear velocity model of the crust and upper mantle, *Geophys. J. Int.*, *151*, 88–105.
Shapiro, N. M., M. H. Campillo, L. Stehly, and M. H. Ritzwoller (2005), High resolution surface wave tomography from ambient seismic noise, *Science*, *307*, 1615–1618.
Shapiro, N. M., and I. Koulakov (2015), Probing the underbelly of a supervolcano, *Science*, vol. 348, pp. 758–759, doi:10.1126/science.aab1828.
Siebert, L., T. Simkin, and P. Kimberly (2010), *Volcanoes of the World*, 3rd ed., 568 p., Univ. of Calif. Press, Berkeley.
Simkin, T., and L. Siebert (1994), *Volcanoes of the World*, 349 pp., Geoscience, Tucson, Ariz.
Troll, V. R., D. R. Hilton, E. M. Jolis, J. P. Chadwick, L. S. Blythe, F. M. Deegan, L. M. Schwarzkopf, and M. Zimmer (2012), Crustal CO_2 liberation during the 2006 eruption and earthquake events at Merapi volcano, Indonesia, *Geophys. Res. Lett.*, *39*, L11302, doi:10.1029/2012GL051307.
Um, J., and C. H. Thurber (1987), A fast algorithm for two-point seismic ray tracing, *Bull. Seism. Soc. Am.*, *77*, 972–986.
Voight, B., E. K. Constantine, S. Siswowidjoyo, and R. Torley (2000), Historical eruptions of Merapi volcano, central Java, Indonesia, 1768–1998, *J. Volcanol. Geotherm. Res.*, *100*(1), 69–138.
Wagner, D., I. Koulakov, W. Rabbel, B.-G. Luehr, A. Wittwer, and H. Kopp (2007), Joint inversion of active and passive seismic data in central Java, *Geophys. J. Int.*, *170*, 923–932, doi:10.1111/j.1365-246X.2007.03435.x.
Walter, T. R., R. Wang, M. Zimmer, H. Grosser, B. Lühr, and A. Ratdomopurbo (2007), Volcanic activity influenced by tectonic earthquakes: Static and dynamic stress triggering at Mt. Merapi, *Geophys. Res. Lett.*, *34*, L05304, doi:10.1029/2006GL028710.
Wölbern, I., and G. Rümpker (2016), Crustal thickness beneath Central and East Java (Indonesia) inferred from P receiver functions, *J. Asian Earth Sci.*, *115*, 69–79.
Young, M. K., N. Rawlinson, P. Arroucau, A. M. Reading, and H. Tkalčić (2011), High -frequency ambient noise tomography of southeast Australia: New constraints on Tasmania's tectonic past, *Geophys. Res. Lett.*, *38*, L13313, doi:10.1029/2011GL047971.
Zhang, H., M. Maceira, P. Roux and C. H. Thurber, (2014), Joint inversion of body-wave arrival times and surface-wave dispersion for three-dimensional seismic structure around SAFOD, *Pure Appl. Geophys.*, *171*, 3013, doi:10.1007/s00024-014-0806-y.
Zulfakriza, Z., E. Saygin, P. R. Cummins, S. Widiyantoro, A. D. Nugraha, B. G. Lühr, and T. Bodin (2014), Upper crustal structure of central Java, Indonesia, from transdimensional seismic ambient noise tomography, *Geophys, J. Int.*, *197*(1), 630–635.